Chapter 6

Results

6.1 DCC: Calculated factorial moments and robust observables

For each real or simulated event, the vertexer returns the number of charged tracks and photons found. Then the frequency distribution for observing a given number of charged and photon-conversion tracks, $\mathcal{N}(n_{ch}, n_\gamma)$, is used to calculate the factorial moments, assuming that the probability of observing an event with a given number of charged tracks and converted photons is given by the observed distribution:

$$P(n_{ch}, n_\gamma) \approx \mathcal{N}(n_{ch}, n_\gamma)/N, \tag{6.1}$$

where N is the total number of events

$$N = \sum_{n_{ch}=0}^{\infty} \sum_{n_\gamma=0}^{\infty} \mathcal{N}(n_{ch}, n_\gamma). \tag{6.2}$$

Statistical errors are estimated assuming Poisson fluctuations and standard propagation of errors formalism. Appendix A shows the derivation of some of the formulas used to calculate uncertainties in the moments and $r_{i,j}$. In order to check the accuracy of the calculated uncertainty in the $r_{i,j}$, the values of $r_{1,1}$ and $\sigma_{r_{1,1}}$ were determined for groups of 25000 events from runs 1096, 1099, 1103, 1109, 1110, 1125, 1126, 1127, 1137, and 1139. Then a Gaussian was fit to the histogram of $(r(i) - \langle r \rangle)/\sigma_r(i)$, where $r(i)$ and $\sigma_r(i)$ are $r_{1,1}$ and $\sigma_{r_{1,1}}$, respectively, for the ith group of events, and $\langle r \rangle = 1.0228$ is the mean $r_{1,1}$ for all events. The fitted Gaussian is shown in Fig. 6.1, and has mean $\mu = 0.012 \pm 0.144$ and standard deviation $\sigma = 0.985 \pm 0.160$. Note that if the calculated uncertainty is equivalent to the actual statistical uncertainty, then the standard deviation of the Gaussian should be $\sigma = 1$. Since this is true to within errors, we believe that the calculated uncertainty accurately represents the true statistical uncertainty.

6.1.1 Simulations

The moments and $r_{i,j}$ were calculated for approximately 1.5×10^5 PYTHIA events which would be seen by the detector (pass trigger cuts) and 2×10^4

pure DCC events, and the results are shown in Table 6.1. The PYTHIA results are given for perfect charged- and photon-finding efficiencies, along with the output of running these events through the GEANT simulation. The DCC events are also processed by the same GEANT simulation, except that the trigger is not used since there are no particles generated in the $\bar{\mathrm{p}}$ direction. For purposes of comparison, the predicted values for idealized binomial and $1/(2\sqrt{f})$ distributions are included. [For $j > 1$, these depend on the parameter ξ, which was estimated using the relationship between $f_{0,2}$, $f_{2,0}$ assuming a binomial distribution. Then the observed $\langle n_\gamma \rangle$ from PYTHIA/GEANT was used to obtain $2\epsilon_2/(\epsilon_1 + 2\epsilon_2) \approx 0.08 \pm 0.01$. The F_i used in these predictions were also determined from the PYTHIA/GEANT data. We do not expect these values to be correct for the DCC case; in particular, the simulated DCC pions have significantly lower $\langle p_T \rangle$ than the PYTHIA pions, so that the detection efficiencies ϵ_1 and ϵ_2 are not the same. However, the values from PYTHIA are used here to illustrate the problems which will arise in DCC searches using these non-robust ratios.]

The $r_{i,1}$ obtained by counting numbers of charged tracks and photons aimed into the acceptance by PYTHIA are within two standard deviations of 1.00. This suggests that something close to a binomial charged-neutral distribution is used by PYTHIA. Detector effects are included by running the events through GEANT. The fact that the lower-order (statistically significant) $r_{i,1}$ did not differ by more than about 10% (and are in fact within

2σ) of the values from the PYTHIA input justifies the claim that the robust observables are indeed insensitive to detection efficiencies, and also that correlations of efficiencies with multiplicities and momentum do not greatly alter the robustness of these variables. The ratios $r_{i,1}$ obtained from running the DCC events through GEANT are somewhat higher than the values predicted for the $1/(2\sqrt{f})$ distribution; however, they are clearly distinguishable from the values for generic production.

The choice of parameters used in the DCC generator is somewhat optimistic; the DCC domain is aimed directly at the center of the acceptance, and the DCC pions have a rather large $\langle p_T \rangle$. As is shown in Fig. 4.17, very low-p_T photons are less likely to convert, and the efficiency for detecting those which do convert is only about 40% for $p_T \lesssim 50$ MeV. Charged pions with low p_T are also more difficult to find because they tend to stop or multiple scatter more in the lead; some scatter so much that the tail is not associated with the head by the vertexer, and may be found as a fake photon conversion. Therefore, we varied the $\langle p_T \rangle$ of the pions in the DCC generator. The resulting moments and $r_{i,j}$ are given in Table 6.2. The parameters in model A are those mentioned previously. Models B and C have lower $\langle p_T \rangle$, 50 MeV and 25 MeV, respectively. In these models, the ratio of mean energy density of the DCC pions to that of generic pions is not changed ($\psi = 1$), which leads to larger numbers of pions in the domain since $\langle N_\pi \rangle \propto \psi / p_T$. In order to keep the mean number of pions constant, we also varied ψ with p_T in models D and E. For DCC domains with very low-p_T pions, the values of the robust observables are closer to what we expect for a binomial distribution, so that distinguishing these domains from generically-produced pions using these observables becomes much more difficult.

Of course, we do not expect to observe events consisting of only a DCC domain aimed into the acceptance. Possible scenarios for mixing DCC and generic multiparticle production are discussed in Ref. [60]. For example, any given event could be due to either DCC or generic production, but not both (exclusive production). Perhaps more realistically, the occurrence of DCC in an event could be independent of the generically-produced pions (independent production), or the amount of DCC production could depend on the amount of generic production (associated production). An example of the latter type is the Baked Alaska model [12], which has the number of DCC pions given by $N_{DCC} \sim {N_{gen}}^{3/2}$.

In order to study the effect of an admixture of DCC with generic events where the amount of DCC produced is independent of the amount of generic production, we added DCC domains from the DCC-generator/GEANT to various fractions of (random) PYTHIA/GEANT events. The effect on the $r_{i,1}$ is shown in Table 6.3. (Note that a slightly older version of the vertexer was used for this study, which accounts for the discrepancy in $r_{1,1}$ here with no DCC added and in Table 6.1.) The values for $r_{i,1}$ fall off faster than linearly with fraction of DCC. For a fraction of 1, i.e. when a DCC domain is added to every event, the ratios are higher than for DCC alone, but are still easily distinguishable from the generic values.

6.1.2 Characteristics of events from lead-in runs

Ten of the lead-in runs (1096, 1099, 1103, 1109, 1110, 1125, 1126, 1127, 1137, and 1139), totaling about 1.5 million events, were used in the following analysis. The running conditions were very clean (e.g. low luminosity) and therefore the diffractive tags had very little contamination from beam-gas interactions. The frequency distribution of events with given numbers of charged tracks and photons is determined (Table 6.4) and used to calculate the factorial moments and $r_{i,j}$. Table 6.5 gives the values for some of these variables. The mean number of charged tracks found per event is about 0.5 and of converted photons is about 0.2. The lower-order $r_{i,1}$ are close to what is expected for a binomial distribution ($r_{i,1} = 1$). The values for $r_{1,1}$ and $r_{1,2}$ are within two standard deviations of the PYTHIA results. The higher-order ratios are weighted towards bins of $\mathcal{N}(n_{ch}, n_\gamma)$ which are statistically limited, and therefore the deviations from unity are not very significant. In any case, the ratios are not smaller than one as would be expected for a contribution from DCC. Therefore the events appear to be consistent with production by only generic mechanisms.

6.1.3 Characteristics of events with diffractive tags

From the 10 runs used in Sec. 6.1.2, 21412 events have a ktag from the scintillator which detected showers from interactions of diffractive anti-protons in the kicker magnets. The mean numbers of charged particles and photons are lower for ktag events, as would be expected for diffractive events, where a large fraction of the total energy is carried away by the beam remnant, and the charged-charged and charged-gamma correlations are correspondingly lower. Table 6.5 gives the values of the $r_{i,j}$ for the ktag events.

The upstream hadronic calorimeters at $z \approx -25\,\mathrm{m}$ are used to tag events with diffractive anti-protons with $x_F \sim 0.5$ and anti-neutrons. Differences related to isospin exchange in diffractive events might be apparent in comparisons between events with an $\bar{\mathrm{n}}$ and those with a $\bar{\mathrm{p}}$. Figure 6.2 shows histograms of the ADC readout from the $\bar{\mathrm{n}}$ and $\bar{\mathrm{p}}$ calorimeters. Events with ADC > 400 (in order to cut out background from products of showers in the magnets) were used to calculate the moments and $r_{i,j}$, given in Table 6.5. The mean number of particles found is higher than that in events with the ktag, but lower than in the total sample of events, and is lower for the tag on leading $\bar{\mathrm{n}}$'s than for $\bar{\mathrm{p}}$'s with half the beam momentum, consistent with energy conservation.

The $r_{i,j}$ for diffractive-tagged events do not differ by more than two standard deviations from the values for the total sample. Therefore, we conclude that there is no evidence for more DCC production in events with diffractive tags, offering no support to the conjecture that Centauros are related to DCC and are diffractive in nature.

6.1.4 Characteristics of events with a pbar multiplicity tag

Since DCC may be more often present in events with large multiplicity, we would like to find a measure of the multiplicity independent of that in the small acceptance. The multiplicity in the scintillator on the downstream anti-proton side of the collision at $z = -81$ in ("pbar counters") may be correlated with the total multiplicity, and therefore could be such a measure.

In GEANT, where the number of charged tracks hitting the pbar counters is known, a plot of the total energy deposited in the pbar counters against the pbar multiplicity (Fig. 6.3) shows the correlation between energy and multiplicity which we expect from minimum-ionizing particles. The pbar multiplicity in the real data can thus be found from the mip peaks in the ADC readout of the counters (Fig. 6.4).

In this way, the pbar multiplicities of events in runs 1099, 1103, 1109, 1125, 1126, and 1127 were determined, and events were grouped in bins of pbar multiplicity, such that each bin contained 10% of the events. The multiplicity in the pbar counters is indeed correlated with that in the acceptance. Table 6.6 shows an increase in $\langle n_{ch} \rangle$ and $\langle n_\gamma \rangle$ with increasing pbar multiplicity. However, the $r_{i,1}$ do not appear to vary with multiplicity, and show no sign of an increased presence of DCC for higher multiplicity events. The $r_{1,1}$'s are consistent with each other and with that for all events.

6.2 Multiparticle analysis

Plots of $dN_{ch}/d\eta$ and $dN_\gamma/d\eta$, uncorrected for detection and trigger efficiencies, are shown in Fig. 6.5 and Fig. 6.6, respectively. The solid line is the result from approximately 1.5×10^6 events from the 10 runs used in previous analysis. The dotted line is the result from the PYTHIA/GEANT simulation, and the dashed line is from the PYTHIA events which passed the GEANT trigger (about 1.5×10^5 events). The charged multiplicity found by the vertexer for GEANT events is higher than that from the PYTHIA input by about 0.15, or 3%. The number of photons found for GEANT is about 42% of the PYTHIA input. The charged multiplicity from the data is lower than that from GEANT and from PYTHIA (about 90% of the GEANT value). The photon multiplicity is approximately 92% of that in GEANT.

Since multiplicity is correlated with NHITS, and the contribution to the NHITS from background is greater in the real data than in GEANT, it is not unlikely that the cut of NHITS < 600 would cut more high-multiplicity events from the data sample than from the GEANT. This conjecture is supported by the results in Sec. 4.3.5, which showed a correlation between pipe shower and multiplicity. However, we do not necessarily expect the data to agree with the simulations, since the PYTHIA input is not based on real measurements at the cm energy and η range of the MiniMax experiment.

6.3 Low p_T photons

There has been controversial evidence suggesting that the number of low-p_T photons produced is larger than what is expected from hadronic decays and QED inner bremsstrahlung, in particular, that there is an excess of photons with $p_T \lesssim 20$ MeV [62]. We have attempted to study this by observing photon conversions in the 1/4 in (0.07 X_0) -thick Al window at $z = 120$ in, and measuring the momentum of the conversion products either by their bending in the scintillator (0.03 X_0-thick at $z = 157$ in) due to multiple scattering or by tracking them into the calorimeter and determining the energy deposited in the hit cells. The lead-out runs were used for this so that the conversion tracks would not stop or scatter and lose energy in the lead. Conversions in the window, rather than in the scintillator, for example, were chosen because the increased resolution in v in the front chambers was desirable for determining the momentum of the converted photon.

First, it was necessary to determine which tracks were due to window conversions. To do this, we plotted the z of closest approach between pairs of tracks. The GEANT lead-out data shows a wide peak at the collision point, and a smaller peak at the window, $z \approx 120$ in, as can be seen in Fig. 6.7. For the real data, the peak at the collision point and at the window are fairly clear, but there is also a smaller peak at intermediate z. This is apparently due to fake tracks made from u wires borrowed from several real tracks, such that the resulting fakes tended to vertex with the real tracks at a location in z between the collision point and the first chamber (which is just behind the window). These fake vertices are removed by requiring the heads to point such that they will hit the lead, and that they hit all eight of the front chambers. The distribution of the z of closest approach for remaining tracks is shown in Fig. 6.8.

A window conversion is defined as a pair of tracks with a z at closest approach between 115 and 150in, and with a reduced χ^2 of the match between the tracks at the window (done in the same way as the usual vertexing at the lead) of $\chi^2/2 < 2.5$ (see Fig. 6.7 for the GEANT distribution and Fig. 6.8 for that of the data). Also, in order to be able to determine the momentum of the conversion tracks by bending in the scintillator or by following them into the calorimeter, each head is required to have exactly one tail which matched to the head with $\chi^2/2 < 5$.

Both conversion tracks are found by the tracker in about 26% of the window conversions in GEANT which send both tracks into the acceptance. Only one track is recorded 70% of the time, usually because the tracks are so close together that they are grouped by the tracker into a single track. This is apparent in Fig. 6.9, which shows the opening angle of window conversion tracks in GEANT and of the pairs of tracks found as window conversions. Conversions with smaller opening angles are much less likely to be found.

Of the pairs of tracks found as window conversions, approximately 90% have one tail matched to each head. As is also shown in Fig. 6.9, the efficiency for finding vertices from the low-p_T photons that convert in the window is fairly high (because such conversions tend to have larger opening angles). Unfortunately, the low-p_T conversion tracks scatter more in the scintillator than high energy particles, so that the efficiency for matching the tails to the heads is relatively low, preventing a determination of the momentum of these tracks.

The momentum of the conversion tracks is determined from the angles between the heads and tails at the scintillator using the relationship between the momentum of a particle and the bending angle of the track due to multiple scattering in a material [36]

$$\theta_0 \approx \frac{13.6\ \mathrm{MeV}}{\beta c p} z \sqrt{\frac{x}{\mathrm{X}_0}}, \tag{6.3}$$

where x/X_0 is the thickness of the material in radiation lengths, p is the momentum and βc the velocity of the particle, z is its charged number, and θ_0 is the bending angle in the plane of the incident and bent track. The momentum of the photons which converted in the window is taken to be the sum of the momenta of the two conversion tracks. The p_T is determined from the total momentum and the angle of the trajectory of the photon, which must have traveled from the collision point to the vertex of the conversion tracks. For GEANT conversions, where the photon momentum is known, the

p_T as determined by bending in the scintillator tends to be lower than the actual p_T (Fig. 6.10). Other attempts to find a measure of the momentum, using, for example, the opening angle, were unsuccessful.

Following the conversion tracks into the calorimeter, their energy is determined to be simply the energy deposited in the cell(s) into which the tracks are aimed, without using a clustering algorithm. The p_t found with this method is surprisingly accurate (Fig. 6.10). Unfortunately, the actual calorimeter was never successfully calibrated, and therefore this method can not be reliably used on the data.

The p_T distributions of "photons" from pairs of tracks which are found as window conversions in the data are shown in Fig. 6.11, although these distributions are not believed to be very accurate. Instead of comparing p_T distributions from GEANT and from the data, a comparison of the number of window conversions integrated over all p_T was used to look for evidence for an excess of low-p_T photons.

First, the origins of pairs of tracks found as GEANT window conversions are determined. The relative contribution from sources other than actual window conversions should be low, and hopefully from sources of similar magnitude in the GEANT and in the data. In a sample of about 10^5 GEANT events, 225 pairs of tracks are identified as window conversions. About half of these really are window conversions (106 conversions in the window and 4 conversions in the first chamber at $z = 123\,\mathrm{in}$). The next largest contribution is 19% from pairs of charged tracks from the collision point which are close together at the window, including 13 dalitz pairs. The large uncertainty in the point of closest approach due to the nearly identical slope of such tracks allows the possibility of their appearing to vertex at the window. Strong interactions in the window, neutral particle decays (e.g. K^0_s, Λ^0), pairs of a primary charged track from the collision and a secondary charged track, and pairs of a charged track and a fake each contribute between 5 and 7% of the pairs found as window conversions. Five events have conversions in the window of secondary photons. The remaining few events involve pairs of secondary tracks from interactions in other material.

Almost 10^6 events from lead-out runs (1089, 1093, 1104, 1108, 1111, 1123, 1124, 1129, 1132) were used to search for window conversions in the data. The ratio of the number of window conversions found in the data to that in GEANT is $2121/339 = 6.3$. The ratio of events in the data sample to that in the GEANT sample is $923238/155737 = 5.9$, so that there appears to be an excess of window conversion in the data of about 6%. The uncertainties involved in this analysis do not allow a precise statement either supporting or contradicting the claim of Ref. [62].

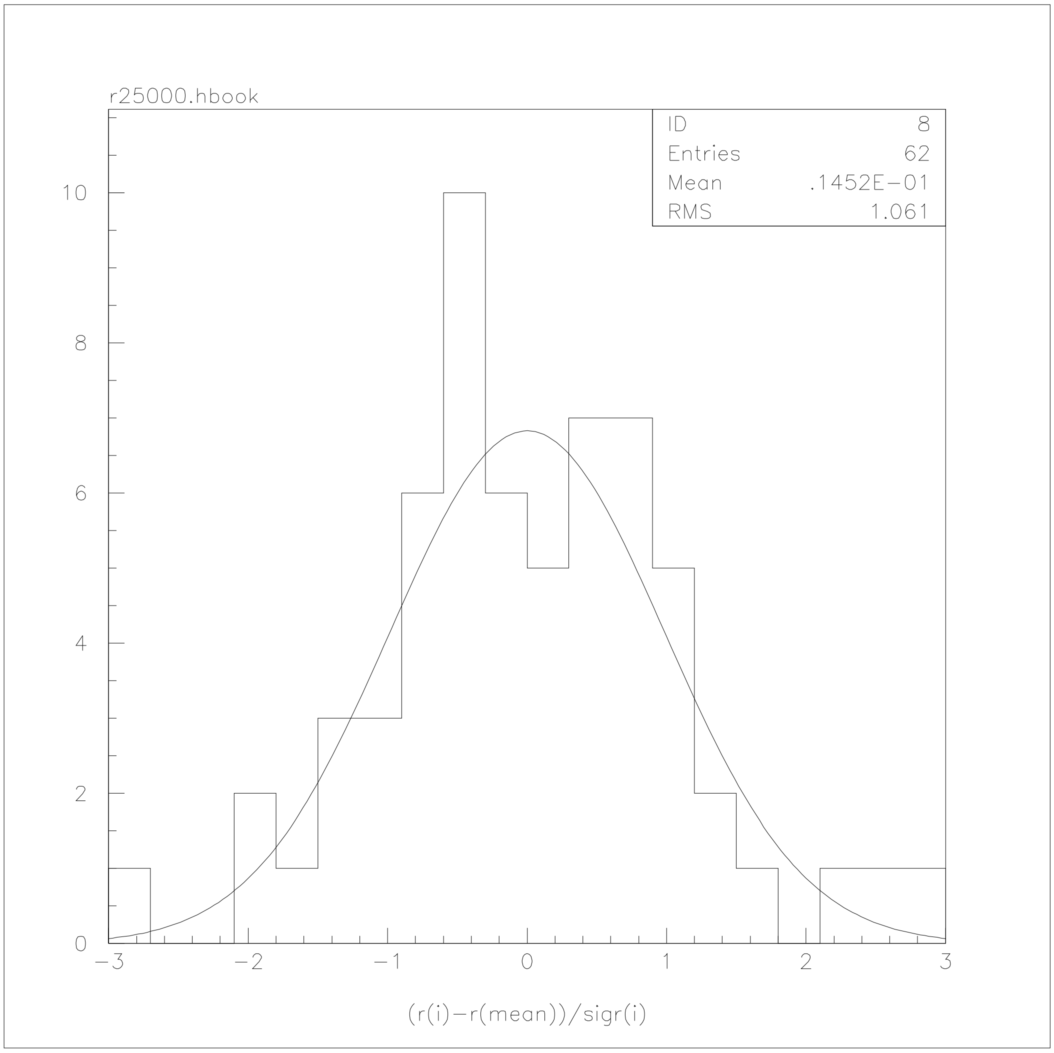

Figure 6.1: Histogram of $(r(i) - \langle r \rangle)/\sigma_r(i)$ for groups (i) of 25000 events and Gaussian fit.

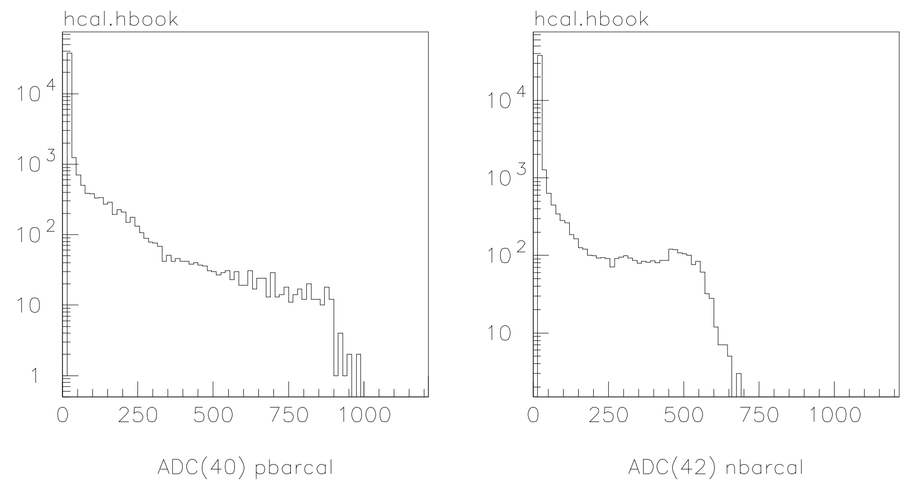

Figure 6.2: ADC values of the hadronic calorimeters which see anti-neutrons [ADC(40)] and anti-protons [ADC(42)].

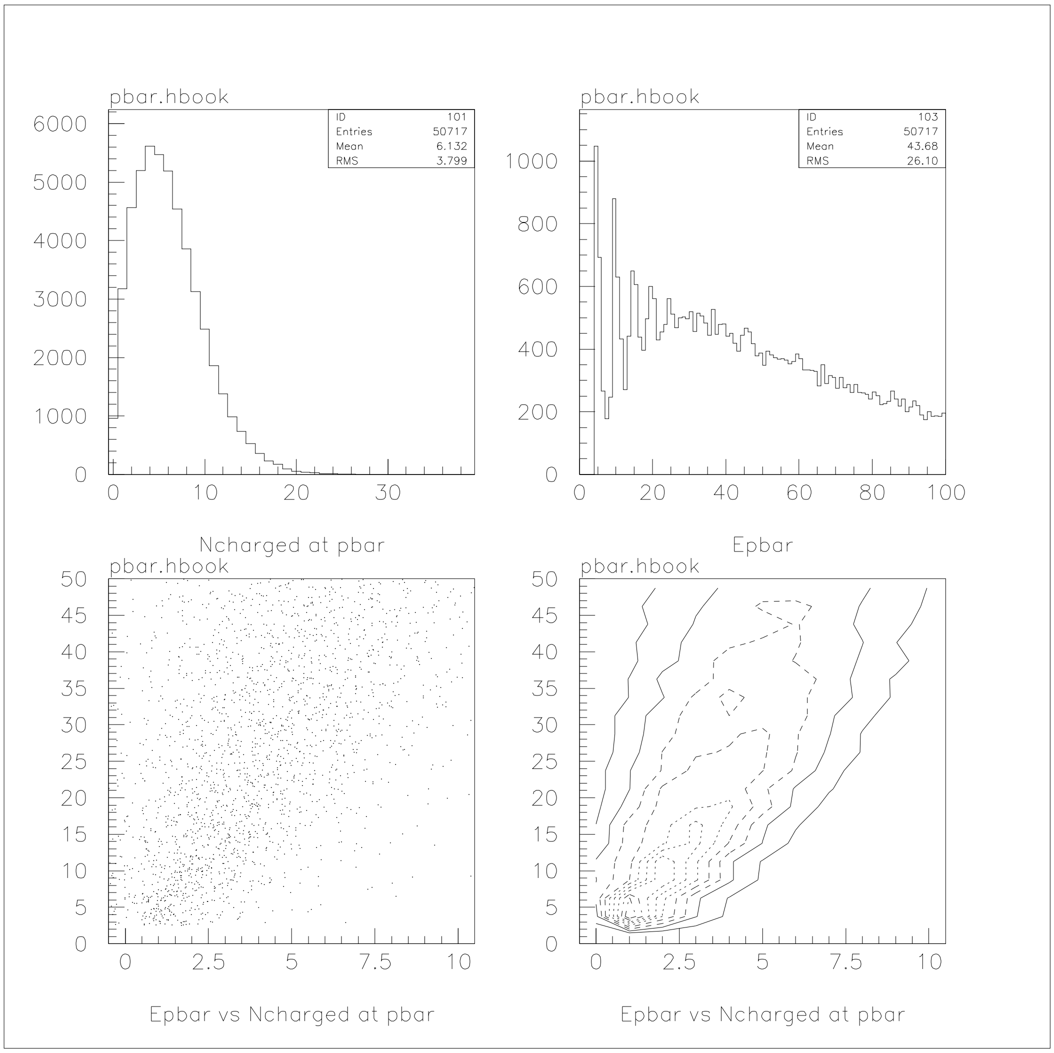

Figure 6.3: Energy (in MeV) deposited in the pbar counters vs number of charged particles hitting these counters

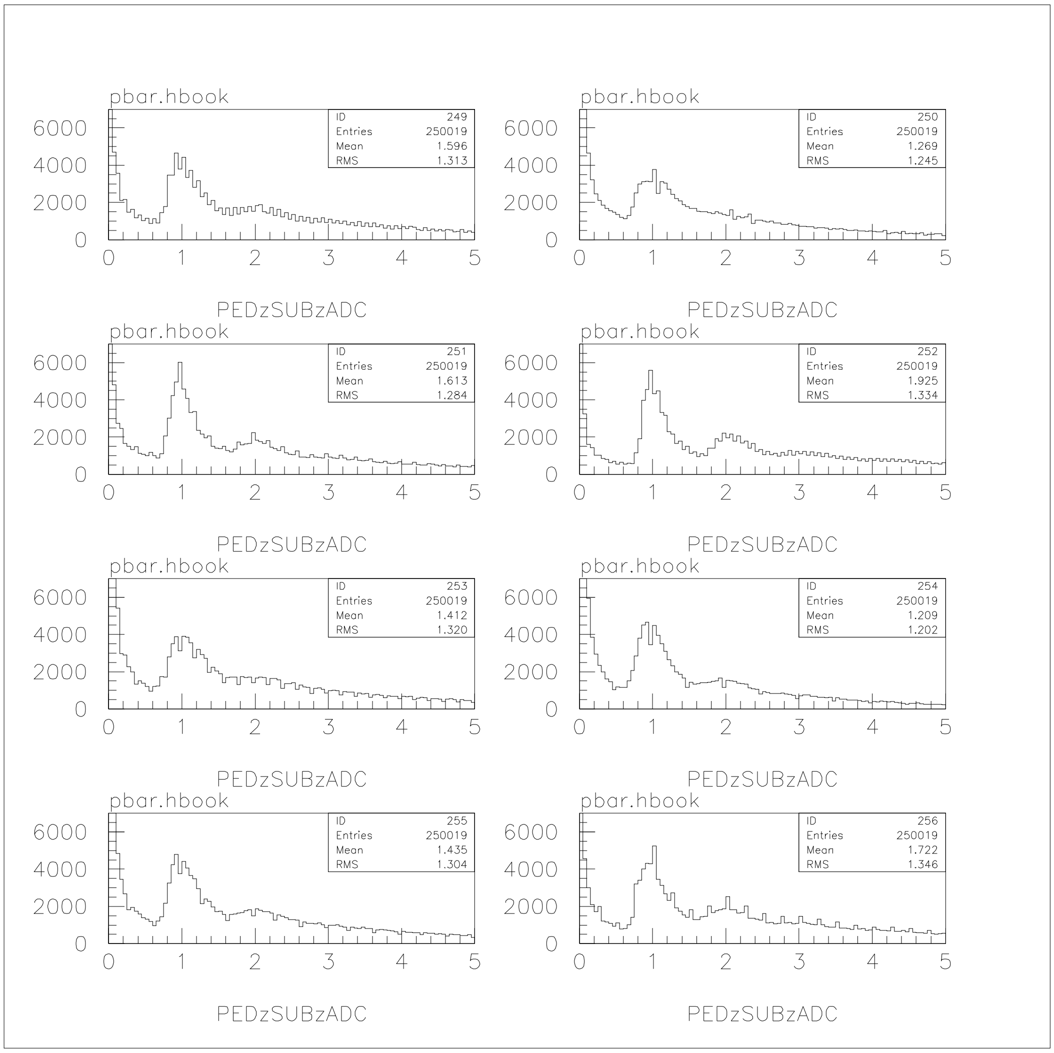

Figure 6.4: PED_SUB_ADC values (in units of mip energies or, equivalently, number of charged particles) of the pbar counters

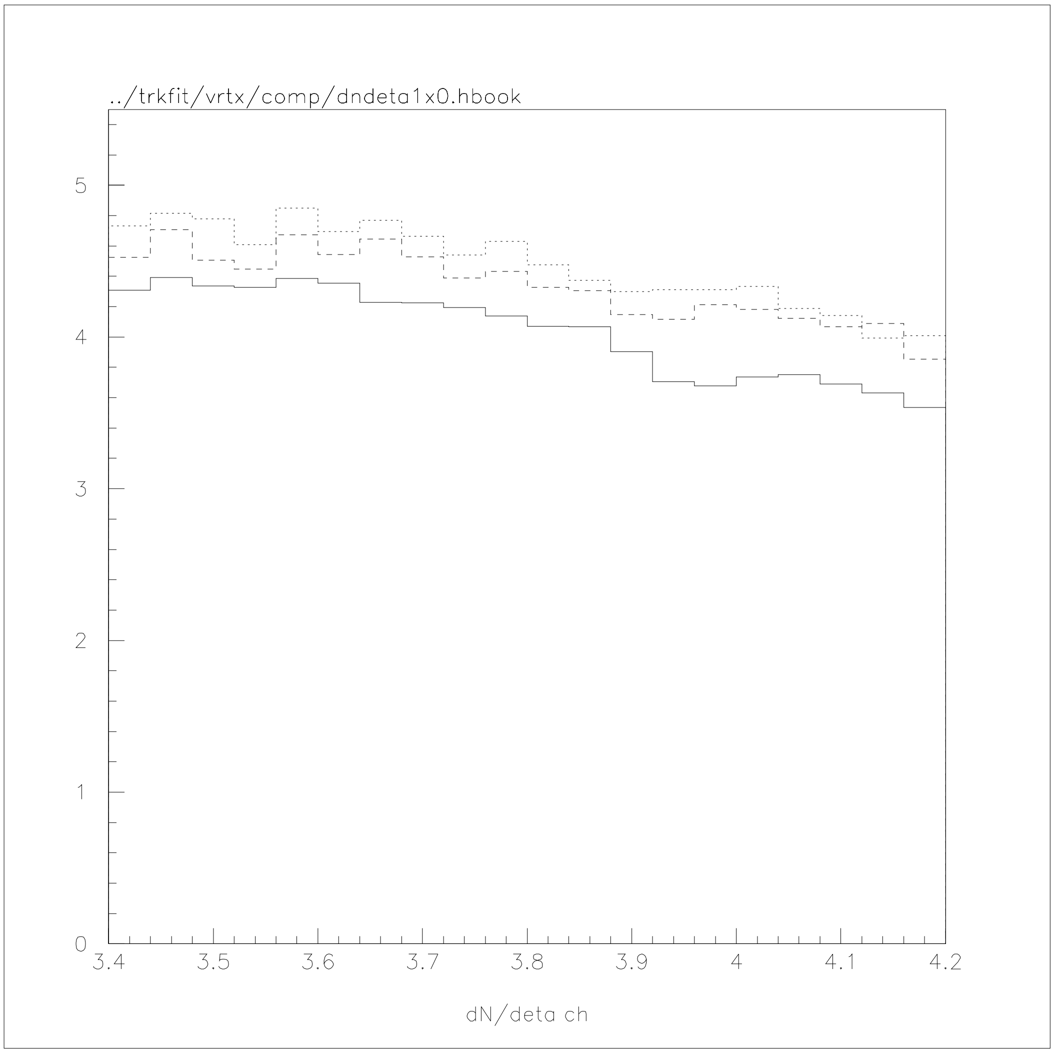

Figure 6.5: Pseudorapidity distribution $dN/d\eta$ vs η for charged tracks in the data (solid), GEANT (dotted), and PYTHIA (dashed), uncorrected for efficiencies.

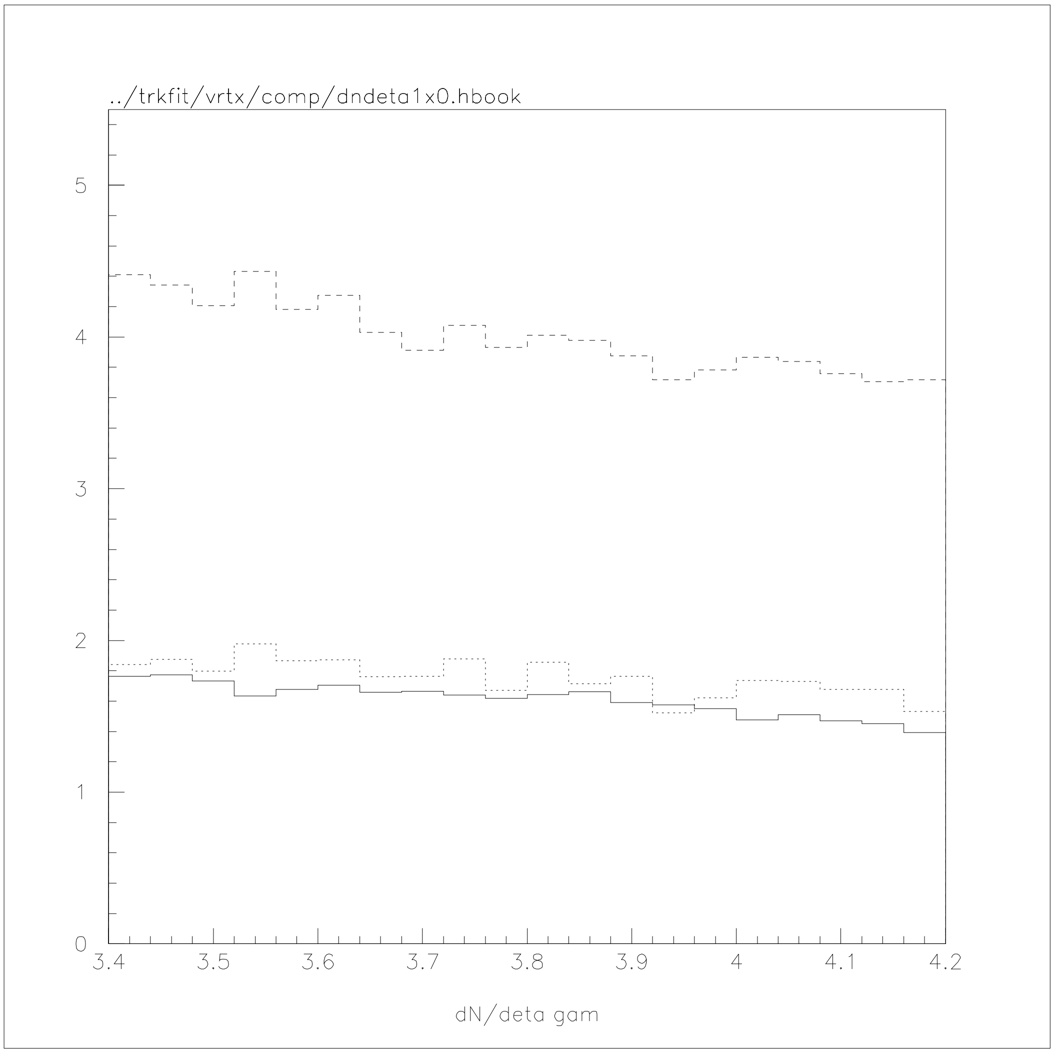

Figure 6.6: Pseudorapidity distribution $dN/d\eta$ vs η for photons in the data (solid), GEANT (dotted), and PYTHIA (dashed), uncorrected for efficiencies.

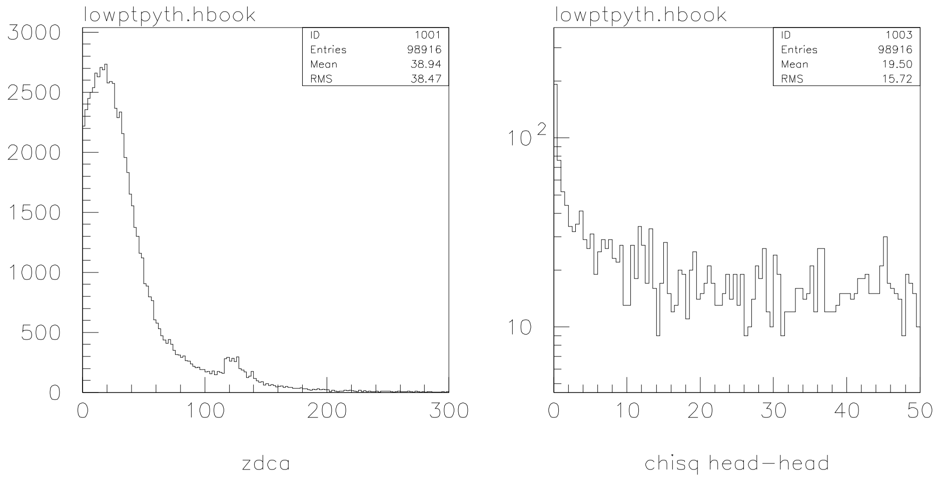

Figure 6.7: Histogram of the z of closest approach between all heads, and of the χ^2 of the matching of those pairs in GEANT.

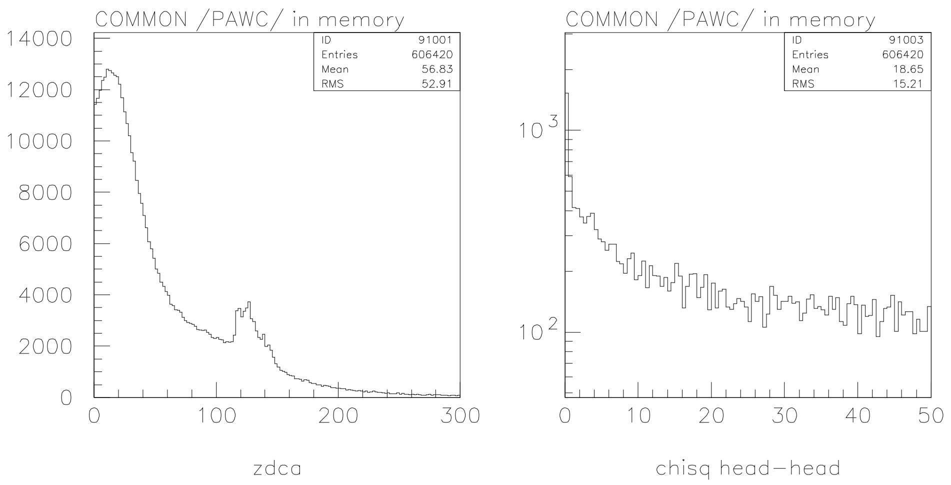

Figure 6.8: Histogram of the z of closest approach between all heads, and of the χ^2 of the matching of those pairs in the data.

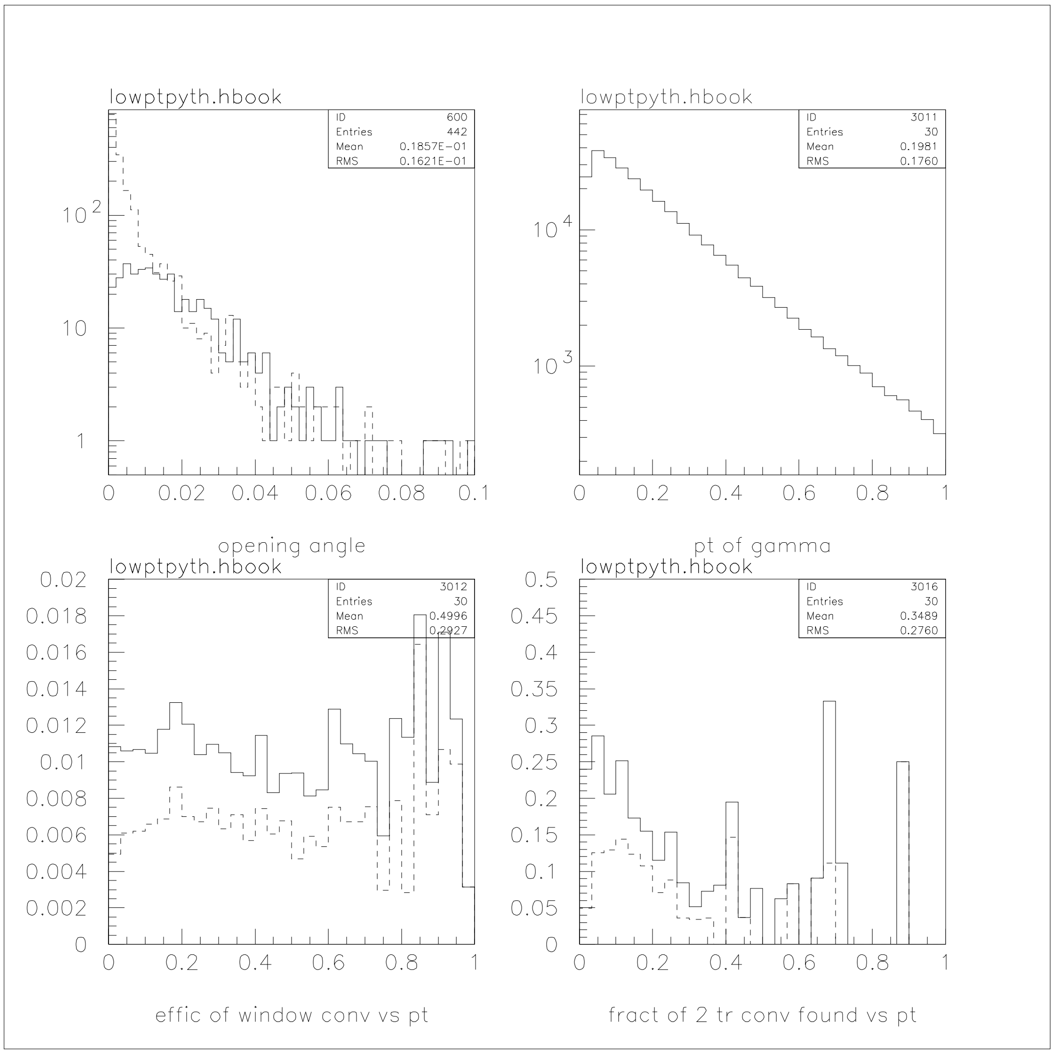

Figure 6.9: Opening angle between pairs found as window conversion tracks in GEANT (solid) and between all GEANT conversion tracks (dashed), p_T of all primary photons in GEANT, and efficiencies for finding window conversions as a function of p_T. In the lower-left plot, the solid line represents the fraction of primary photons which converted in the window, the dashed line is the fraction which also produced two conversion tracks in the acceptance. In the lower right plot, the solid line is the fraction of window conversions with both tracks in the acceptance which were found as a pair of heads, and the dashed line is the fraction which also had one tail per head.

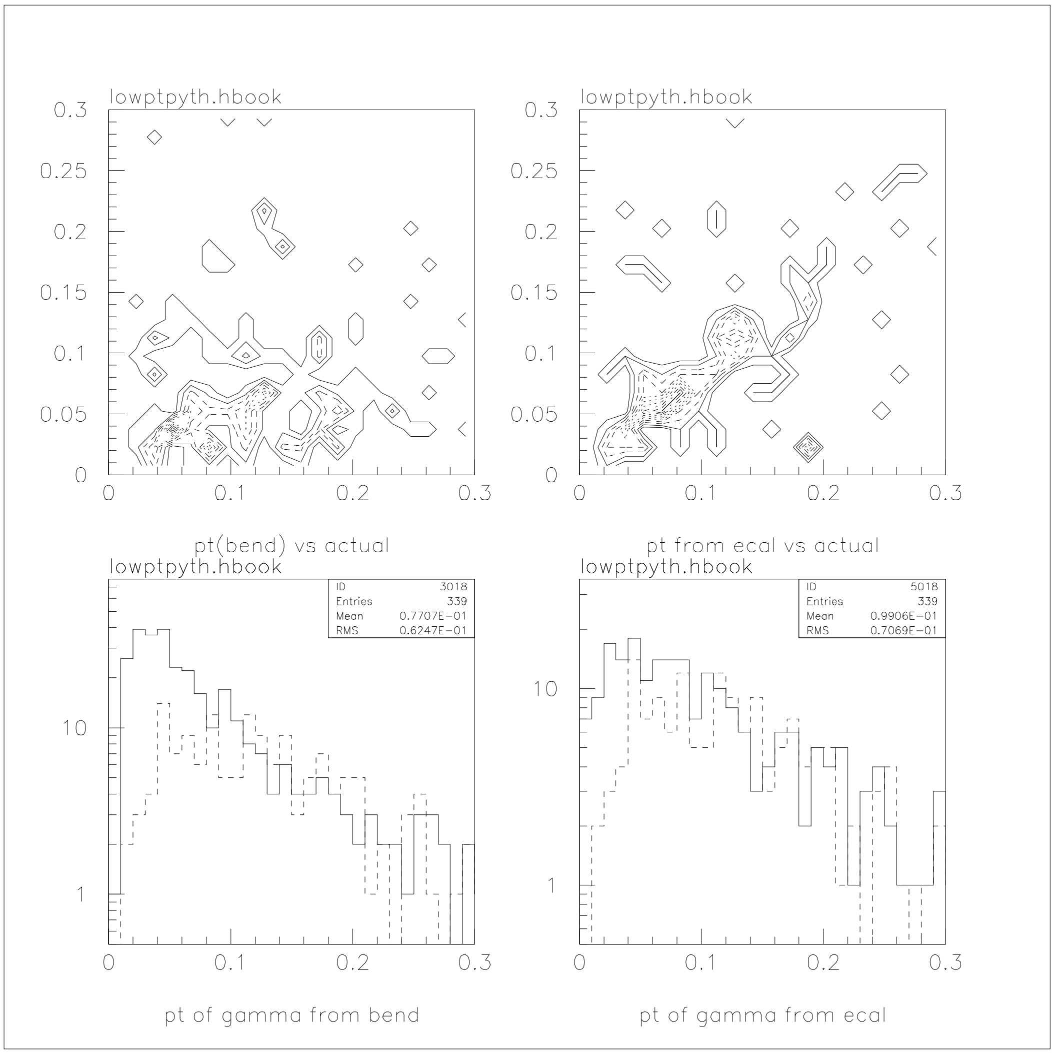

Figure 6.10: Contour plots of the p_T found by bending in the scintillator and by using the calorimeter vs the actual p_T of the converted photon in GEANT, and corresponding p_T distributions (solid is calculated p_T, dashed is actual).

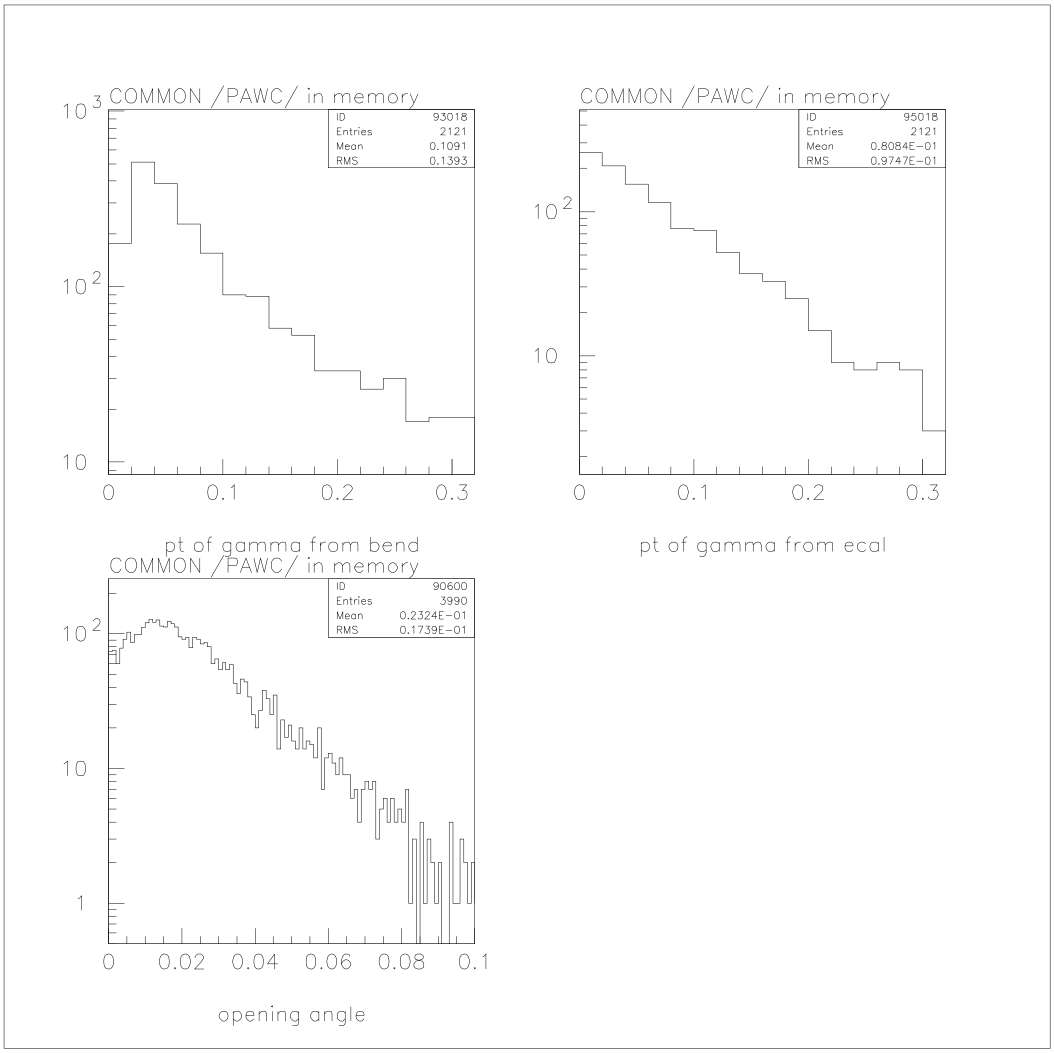

Figure 6.11: Distributions of p_T found by bending in the scintillator and by using the calorimeter for converted photons in the data.

		PYTHIA	PYTHIA/GEANT	DCC/GEANT	binomial	$1/(2\sqrt{f})$
i	j	$r_{ij} \pm \sigma_{r_{ij}}$	$r_{ij} \pm \sigma_{r_{ij}}$	$r_{ij} \pm \sigma_{r_{ij}}$	r_{ij}	r_{ij}
1	1	1.00 ± 0.01	1.00 ± 0.01	0.58 ± 0.01	1.00	0.50
2	1	0.99 ± 0.02	1.00 ± 0.03	0.44 ± 0.03	1.00	0.33
3	1	0.96 ± 0.06	1.03 ± 0.07	0.39 ± 0.05	1.00	0.25
4	1	1.02 ± 0.11	1.29 ± 0.18	0.42 ± 0.11	1.00	0.20
5	1	1.32 ± 0.20	2.03 ± 0.56	0.51 ± 0.37	1.00	0.17
6	1	2.06 ± 2.52	3.61 ± 1.35	0.51 ± 0.73	1.00	0.14
0	2	1.24 ± 0.01	1.36 ± 0.02	1.51 ± 0.05	1.36	1.80
1	2	1.20 ± 0.04	1.37 ± 0.05	0.67 ± 0.05	1.30	0.62
2	2	1.13 ± 0.09	1.45 ± 0.15	0.43 ± 0.08	1.25	0.31
0	3	1.60 ± 0.06	2.35 ± 0.15	2.77 ± 0.34	1.89	3.54
1	3	1.50 ± 0.15	2.47 ± 0.30	1.17 ± 0.27	1.74	0.90
0	4	2.09 ± 0.24	4.82 ± 0.86	6.04 ± 1.84	2.70	7.34

Table 6.1: Robust observables $r_{i,j}$ for generic events simulated by PYTHIA and pure-DCC events simulated by the DCC generator, along with predictions for binomial and $1/(2\sqrt{f})$ distributions.

model	A	B	C	D	E
# events	20000	10000	10000	10000	10000
$\langle p_T \rangle$ (MeV)	100	50	25	50	25
ψ	1	1	1	0.5	0.25
$\langle N_\pi \rangle$	5.0	10.0	19.9	5.0	5.0
$\langle n_{ch} \rangle$	0.97 ± 0.01	1.96 ± 0.02	2.98 ± 0.02	0.99 ± 0.01	0.93 ± 0.01
$\langle n_\gamma \rangle$	0.27 ± 0.01	0.29 ± 0.01	0.33 ± 0.01	0.14 ± 0.01	0.06 ± 0.01
$\langle n_{ch}(n_{ch}-1) \rangle$	1.03 ± 0.02	4.22 ± 0.07	9.43 ± 0.11	1.08 ± 0.03	0.94 ± 0.02
$\langle n_{ch} n_\gamma \rangle$	0.17 ± 0.01	0.43 ± 0.01	1.03 ± 0.02	0.09 ± 0.01	0.05 ± 0.01
$r(1,1)$	0.58 ± 0.01	0.69 ± 0.01	0.97 ± 0.01	0.62 ± 0.02	0.83 ± 0.05
$r(2,1)$	0.44 ± 0.03	0.61 ± 0.03	1.03 ± 0.02	0.48 ± 0.05	0.92 ± 0.11
$r(3,1)$	0.39 ± 0.05	0.57 ± 0.04	1.12 ± 0.04	0.39 ± 0.08	1.07 ± 0.28
$r(0,2)$	1.51 ± 0.05	1.27 ± 0.06	1.06 ± 0.04	1.32 ± 0.12	1.52 ± 0.31
$r(1,2)$	0.67 ± 0.05	0.64 ± 0.05	1.10 ± 0.06	0.61 ± 0.10	0.79 ± 0.30
$r(2,2)$	0.43 ± 0.08	0.41 ± 0.06	1.27 ± 0.09	0.34 ± 0.13	0.75 ± 0.44
$r(0,3)$	2.77 ± 0.34	2.08 ± 0.34	1.17 ± 0.21	2.52 ± 0.95	3.06 ± 3.04
$r(1,3)$	1.17 ± 0.27	0.79 ± 0.16	1.24 ± 0.24	0.75 ± 0.38	0.00 ± 0.00
$r(0,4)$	6.04 ± 1.84	3.81 ± 1.49	1.66 ± 0.98	5.41 ± 5.42	0.00 ± 0.00

Table 6.2: Results for varying parameters in the DCC generator.

fraction	$r_{1,1} \pm \sigma_{r_{1,1}}$	$r_{2,1} \pm \sigma_{r_{2,1}}$	$r_{3,1} \pm \sigma_{r_{3,1}}$	# events
0.00	1.01 ± 0.02	1.02 ± 0.05	1.09 ± 0.14	51471
0.02	1.00 ± 0.02	1.00 ± 0.05	1.01 ± 0.15	51741
0.05	0.97 ± 0.02	0.93 ± 0.05	0.95 ± 0.10	51741
0.10	0.95 ± 0.02	0.89 ± 0.04	0.89 ± 0.08	51741
0.20	0.93 ± 0.02	0.83 ± 0.04	0.77 ± 0.07	51741
0.50	0.84 ± 0.01	0.71 ± 0.03	0.68 ± 0.06	40000
1.00	0.74 ± 0.01	0.60 ± 0.03	0.55 ± 0.06	20000

Table 6.3: The effect on the $r_{i,1}$ of an admixture of DCC and generic (PYTHIA) events. DCC domains from the DCC generator/GEANT are added to various fractions of random PYTHIA/GEANT events. The first column represents the fraction of events in which a DCC is overlaying a generic event. A DCC fraction of 1 means that DCC has been added to every event, not that the events are pure DCC as in Table 6.1.

		n_γ 0	1	2	3	4	5	6	7	8
	0	834625	126160	16739	2515	454	67	10	8	1
	1	355999	62717	10398	1732	272	56	12	1	0
	2	87117	19140	3580	639	148	31	4	0	0
	3	17786	4771	1016	208	34	9	0	0	0
n_{ch}	4	3350	943	224	48	10	2	0	0	0
	5	516	182	49	7	4	0	0	0	0
	6	88	38	7	3	0	0	0	0	0
	7	10	6	1	0	0	0	0	0	0
	8	0	1	0	0	0	0	0	0	0

Table 6.4: Number of events with a given n_{ch}, n_γ.

	all events	ktag	n̄ hcal	p̄ hcal
# events	1551738	21412	27807	42449
$\langle n_{ch} \rangle$	0.4814 ± 0.0006	0.407 ± 0.005	0.422 ± 0.004	0.437 ± 0.003
$\langle n_{\gamma} \rangle$	0.1922 ± 0.0004	0.167 ± 0.003	0.173 ± 0.003	0.183 ± 0.002
$\langle n_{ch}(n_{ch} - 1) \rangle$	0.2830 ± 0.0010	0.195 ± 0.007	0.213 ± 0.006	0.227 ± 0.005
$\langle n_{ch} n_{\gamma} \rangle$	0.1156 ± 0.0004	0.084 ± 0.003	0.092 ± 0.003	0.103 ± 0.002
$r(1,1)$	1.0228 ± 0.0035	1.052 ± 0.036	1.051 ± 0.031	1.076 ± 0.024
$r(2,1)$	1.0320 ± 0.0097	1.134 ± 0.107	1.042 ± 0.083	1.116 ± 0.069
$r(3,1)$	1.0563 ± 0.0251	1.302 ± 0.281	1.220 ± 0.211	1.180 ± 0.173
$r(4,1)$	1.1183 ± 0.0612	1.802 ± 0.637	2.102 ± 0.599	1.370 ± 0.413
$r(5,1)$	1.3382 ± 0.1436			1.721 ± 0.911
$r(6,1)$	2.0758 ± 0.4159			
$r(7,1)$	5.0105 ± 5.6885			
$r(0,2)$	1.5793 ± 0.0092	1.647 ± 0.090	1.683 ± 0.077	1.658 ± 0.059
$r(1,2)$	1.5632 ± 0.0204	1.623 ± 0.217	1.700 ± 0.176	1.675 ± 0.152
$r(2,2)$	1.5538 ± 0.0497	1.914 ± 0.616	1.908 ± 0.474	1.933 ± 0.441
$r(0,3)$	3.3711 ± 0.0759	3.378 ± 0.627	3.359 ± 0.545	3.333 ± 0.390
$r(1,3)$	3.1115 ± 0.1210	3.335 ± 1.165	3.196 ± 0.895	3.367 ± 0.958
$r(0,4)$	8.9729 ± 0.6201	6.675 ± 2.934	7.266 ± 2.980	6.236 ± 1.780

Table 6.5: Values of $r_{i,j}$ for all lead-in events and for those with diffractive tags.

bin	$\langle n_{ch} \rangle$	$\langle n_\gamma \rangle$	$r_{1,1}$	$r_{2,1}$	$r_{3,1}$
1	0.364 ± 0.002	0.145 ± 0.002	1.02 ± 0.02	0.97 ± 0.06	0.87 ± 0.14
2	0.401 ± 0.002	0.165 ± 0.002	1.00 ± 0.02	1.00 ± 0.05	1.04 ± 0.14
3	0.426 ± 0.002	0.173 ± 0.002	1.03 ± 0.02	1.11 ± 0.05	1.28 ± 0.13
4	0.449 ± 0.002	0.183 ± 0.002	1.00 ± 0.02	1.05 ± 0.05	1.10 ± 0.13
5	0.468 ± 0.003	0.190 ± 0.002	1.03 ± 0.02	1.10 ± 0.05	1.17 ± 0.14
6	0.493 ± 0.003	0.195 ± 0.002	1.02 ± 0.02	1.01 ± 0.04	1.05 ± 0.11
7	0.503 ± 0.003	0.202 ± 0.002	1.04 ± 0.02	1.03 ± 0.05	0.98 ± 0.12
8	0.531 ± 0.003	0.215 ± 0.002	1.01 ± 0.01	1.00 ± 0.04	0.97 ± 0.09
9	0.555 ± 0.003	0.221 ± 0.002	1.03 ± 0.01	1.06 ± 0.04	1.09 ± 0.11
10	0.603 ± 0.003	0.237 ± 0.002	1.03 ± 0.01	1.02 ± 0.03	1.01 ± 0.07

Table 6.6: Mean multiplicities and robust observables for bins of pbar multiplicities each containing 10% of the events. The pbar multiplicity increases with increasing bin number 1-10.

Chapter 7

Conclusions

MiniMax ran successfully with many different detector configurations for a period of about two years. During this time, much was learned which should prove useful for the operation and design of future detectors in the forward region. More than 1.5×10^6 events with lead in and almost 10^6 events with lead out from clean runs when the detector was running properly have been analyzed for the work presented here.

The GEANT simulation does not accurately represent the amount of background seen in the wire chambers from interactions in material surrounding the detector. Even with all of the material included in the simulation, the mean number of hits in the MWPC's is low by about a factor of two. However, the PYTHIA/GEANT output is useful for setting upper limits on how well the data analysis tools are able to reconstruct events. Based on the efficiencies and numbers of fakes discussed in Sec. 4.3, the tracker and vertexer appear to work quite well.

The simulations also show that the robust observables of Chapter 5 are insensitive to detector effects and physics complications, as advertised. The PYTHIA/GEANT simulation, which includes a photon conversion efficiency of slightly better than 50%, an efficiency of 80% for detecting converted photons, resonance production, simulations of detector effects, and many other features, matches the predictions of a simple binomial model. At least for DCC modeled as in Sec. 3.3, the robust observables should be useful in distinguishing DCC from generic production.

We have found no evidence for DCC in the total sample of events or in diffractive events. Limits on the amount of DCC which could be present without being detected depend on the models of DCC (e.g. the p_T of the DCC pions) and of combining DCC with generic production.

Raw measurements of $dN_{ch}/d\eta$ and $dN_\gamma/d\eta$ have been made in a previously unexplored region of phase space, from which actual distributions can be derived, taking into account detection efficiencies and fakes, and trigger efficiencies. Further work on modeling fakes in the data is necessary before this can be done.